


Cavity dynamics and vibrations of a flexible hydrofoil in the cavitating flow

Yunqing Liu ¹, Qin Wu,¹ Hanzhe Zhang,² and Biao Huang^{1,*}¹*School of Mechanical Engineering, Beijing Institute of Technology, Beijing 100081, China*²*Aviation Engineering School, Air Force Engineering University, Xi'an 710051, China*

(Received 18 September 2023; accepted 28 November 2023; published 23 January 2024)

The objective of this paper is to investigate the influence of fluid-structure interaction on the cavity dynamics and the vibrations around a flexible hydrofoil by comparing the experimental results of a rigid hydrofoil. Cavitation behavior, vibrations, and lifts are obtained by a synchronized measured system utilizing a high-speed camera, lift measurement, and a portable laser vibrometer. The nose-up twisting deformation results in an increase in the effective angle of attack, which leads to an increase in cavity length and a reduction of cloud cavity shedding frequency. It also accelerates the transition of the cavitation regimes and shedding mechanism of cloud cavities with the decrease in cavitation number, together with the amplification of vibration velocity, and the suppression of higher-frequency oscillations.

DOI: [10.1103/PhysRevFluids.9.014304](https://doi.org/10.1103/PhysRevFluids.9.014304)

I. INTRODUCTION

Cavitation generally occurs when the local pressure drops below the saturated vapor pressure with the vapor generated in a flowing fluid [1]. When it happens in a marine propulsor, it causes erosion, vibration, noise, and even structural failure [2–4]. With the development of hydraulic engineering, hydraulic machinery is being developed toward large size, large capacity, high speed, and high performance, and the above problems caused by traditional metal materials have gradually become prominent. Lightweight, flexible marine structures have been used in the marine engineering and naval industry due to their resistance to both corrosion fatigue and cavitation erosion, long life, and weight loss [5]. With the use of lightweight structures in those fields, the structure deforms obviously under cavitating flows, and the deformation also affects cavitation development. Therefore, the fluid-structure interaction (FSI) in cavitating flow becomes more complex.

For many years, extensive experiments and simulations have been conducted to study the effect of cavitation on the hydroelastic response of the hydrofoil, such as vibration and pressure pulsion hydrodynamic loads, and deformations [6–9]. Cavitation induces a large increase in the vibration and deformations under unstable hydrodynamic loading of the flexible hydrofoil [10,11], and the high-amplitude fluctuations of the hydrodynamic loading interacting with a flexible body can induce strong fluid-structure interactions and instabilities [12–14]. In addition, the main frequencies of the deformation and vibration frequency spectrum of the flexible hydrofoil are not only associated with the natural frequencies and cavity shedding frequency [15,16] but also related to n times the natural frequency due to the reduced natural frequency of the flexible hydrofoil [17]. Liu *et al.* [18] elucidated the effect of FSI on the hydrodynamic loads and vibration frequencies around a flexible hydrofoil and a rigid hydrofoil with the same undeformed geometries. The nose-up deformation of the flexible hydrofoil results in an increase in the lift and moment coefficients. The main vibration frequencies also include small-scale vortex shedding frequencies. Smith *et al.* [19] found that the

*Corresponding author: huangbiao@bit.edu.cn

reduced stiffness causes secondary lock-in of the flexible hydrofoil's one-quarter subharmonic when the cavitation number is smaller, in addition to another lock-in of the first structural mode with a larger range of cavitation numbers.

In addition to the influence of cavitation on the hydroelastic response, deformations and vibrations of the hydrofoil also influence the cavity dynamics [20], and the transition of the flow field [21,22]. In addition, nose-up deformation accelerates the cavitation inception and transition from sheet cavitation to cloud cavitation and increases the cavity length, resulting in a reduction in shedding frequency [18]. Vibrations cause the cavities around a flexible hydrofoil to be more fragmented [23]. Smith *et al.* [24] found that the cavity at the tip of the hydrofoil did not have as strong a periodicity as the rigid hydrofoil by comparing the spanwise space-time diagram, which was due to the force-induced tip displacement imposed by the cavity shedding from the tip end interfering with the shedding physics at the tip end.

The literature review above provides much information on the FSI problems of a flexible hydrofoil, but experimental observations are still required for a better understanding of this complex FSI phenomenon from a global perspective of cavitation regimes and to provide experimental data. Consequently, the objective of this work is to investigate the effect of FSI on the cavitation and hydroelastic response of a flexible hydrofoil by comparing the results from a rigid hydrofoil with the same geometry.

II. EXPERIMENTAL METHODS

A. Experimental setups

Testing was conducted in the École Polytechnique Fédérale de Lausanne (EPFL) high-speed cavitation tunnel [25]. The tunnel mainly consists of the inlet pipe, the constricted section, the test section (0.75 m long, 0.15 m wide, and 0.15 m high), the return pipe, and the diffusion section. A simultaneous sampling system combining high-speed camera visualization with a sampling frequency of 10 000 fps, lift measurement, and vibration measurement with a sampling frequency of 10 000 Hz is applied in the present work. The vibration measurement point is selected in the midspan behind the center of the chord ($x/c = 0.6$) on the pressure side of the hydrofoil. Measurements were repeated for the flexible hydrofoil under the same conditions as for the rigid hydrofoil, where it was mounted at a fixed incidence, α , of 3° and tested at the upstream velocity U_∞ , equal to 11 m/s. The cavitation number $\sigma = 2(p_\infty - p_v)/\rho U_\infty^2$, where p_∞ is the tunnel pressure measured at the test section inlet, p_v is the saturated vapor pressure, and ρ is the fluid density, which varies from 0.27 to 1.74. More details about the experimental setup can be found in our previous work on a rigid hydrofoil [26].

B. Test hydrofoils

The flexible hydrofoil features an undeformed geometry identical to that of the stainless-steel hydrofoil described in our previous study [26] with a blunt truncated NACA 0009 hydrofoil, with a chord length c of 100 mm, trailing edge thickness h of 3.22 mm, and span s of 149 mm. It is made of polyacetal (POM), with a density $\rho_s = 1480$ kg/m³, modulus of elasticity $E = 3$ GPa, and Poisson coefficient $\mu = 0.35$. The position of the flexible hydrofoil in the water tunnel test section is the same as that of the rigid hydrofoil. The center of the hydrofoil is located at a point two-thirds of the distance from the inlet of the test section. The gap between the hydrofoil and the wall of the water tunnel is 1 mm.

The correlation method is applied in the present work to measure the small deflection of the leading edge and trailing edge. The correlation method is a matching algorithm based on image gray scale. Image matching refers to an imaging technology that finds the subimage most similar to the real-time image in the subimage set of the known target reference image, to achieve the purpose of target recognition and positioning. It is based on the normalized cross-correlation (NCC) coefficient between two images. The NCC has values between 0.0 and 1.0. When the NCC is 1.0,

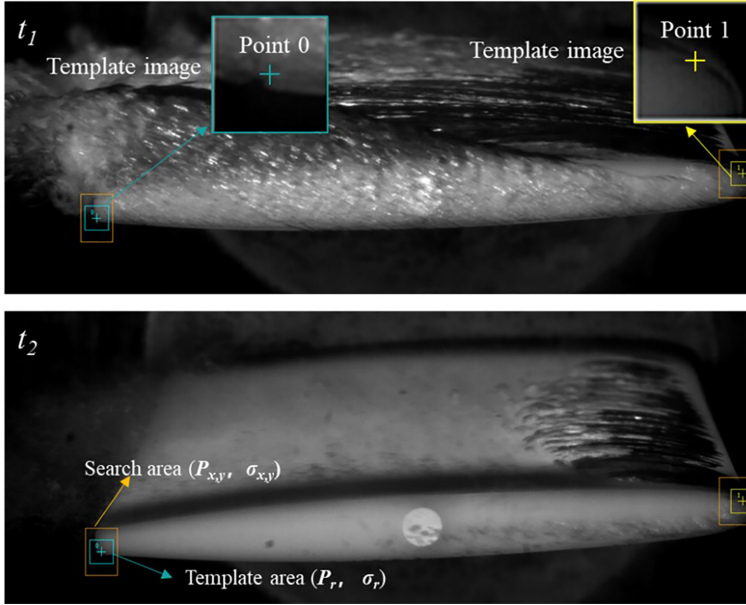


FIG. 1. Correlation method to measure the small deflection of the flexible hydrofoil. It is based on the normalized cross correlation (NCC) coefficient between two images. Two points are selected to represent the deflections of leading edge and trailing edge.

the current image exactly matches the reference image. The normalized cross-correlation (NCC) coefficient can be written as

$$\rho_{xy} = \text{cov}(P_{x,y}, P_r) / \sigma_{x,y} \sigma_r, \quad (2.1)$$

where P_{xy} represents the sub-block in the “search area” with (x, y) as the upper left point and the same as the “template area.” $\sigma_{x,y}$ is the standard deviation of the search area and σ_r is the standard deviation of the template area; $\text{cov}(P_{x,y}, P_r)$ is the covariance of the search area between two adjacent images, and can be written as follows:

$$\text{cov}(P_{xy}, P_r) = E[(P_{xy} - E[P_{xy}])(P_r - E[P_r])] = E[P_{xy}P_r] - E[P_{xy}]E[P_r]. \quad (2.2)$$

Two points (point 0 and point 1) shown in Fig. 1 are selected as the basis to measure the bending and twisting deformation of the flexible hydrofoil. The center of the template area was determined when the point was specified, which defines how large an area of the “template image” is to be searched for and tracked. The template image displays an image of the tracking template, as shown in the blue and yellow boxes. The search area limits the scope of the search, as shown in the origin box. It defines how large an area is to be searched, in the next image, for template image matches. Typically, these values are set to two to three times the size of the initial image template. Once the location of the template area is changed, the location of the search area is changed to ensure that its center always matches the center of the template area. Tracking sensitivity defines the acceptable level of difference between the template and the occurrence in the new image; 0.8 is applied in the present work.

The bending and twisting deformations are based on the center of the chord. According to the coordinate of the leading edge and trailing edge measured by the correlation method, the bending deformation h and twisting deformation θ can be calculated by the equation shown in Fig. 2.

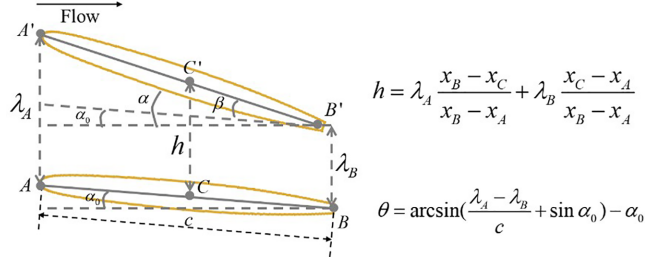


FIG. 2. Schematic of the bending and twisting deformation of the flexible hydrofoil. The bending deformation is represented by the distance between point C and point C' , which is based on the center of the hydrofoil. The twisting deformation θ is the rotation of the profile centerline from the zero-load case where α_0 is the original angle of attack, and λ_A and λ_B are the distances between points A and A' , and points B and B' , respectively.

III. RESULTS AND DISCUSSIONS

A. Global cavity dynamics and vibrations

The average maximum and minimum value of attached cavity length l over all periods normalized by the chord length c of two hydrofoils obtained with different cavitation numbers σ ranging from 0.3 to 1.5 together with bending and twisting deformations of the flexible hydrofoil are shown in Fig. 3, where the attached cavity length is defined from the leading edge to the cavity closure based on the middle span of the hydrofoil, and it is annotated in the top view of the cavity structures.

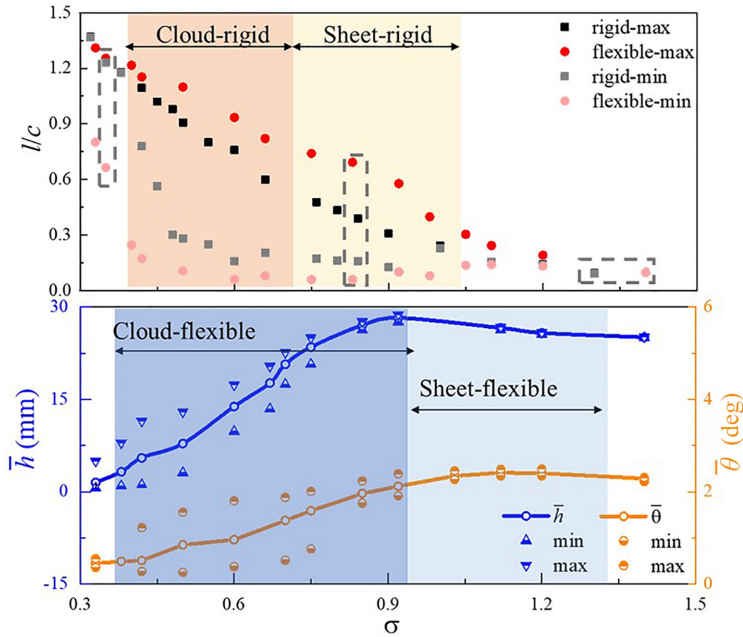


FIG. 3. Dimensionless maximum and minimum attached cavity length l/c against cavitation number σ and maximum, minimum, and mean values of bending \bar{h} and twisting deformations $\bar{\theta}$ of the flexible hydrofoil. The origin area and the yellow areas in the cavity length diagram are the cloud cavitation and sheet cavitation regimes of the rigid hydrofoil, respectively. The dark blue and light blue regions in the deformation diagram are the cloud cavitation and sheet cavitation regimes of the flexible hydrofoil, respectively.

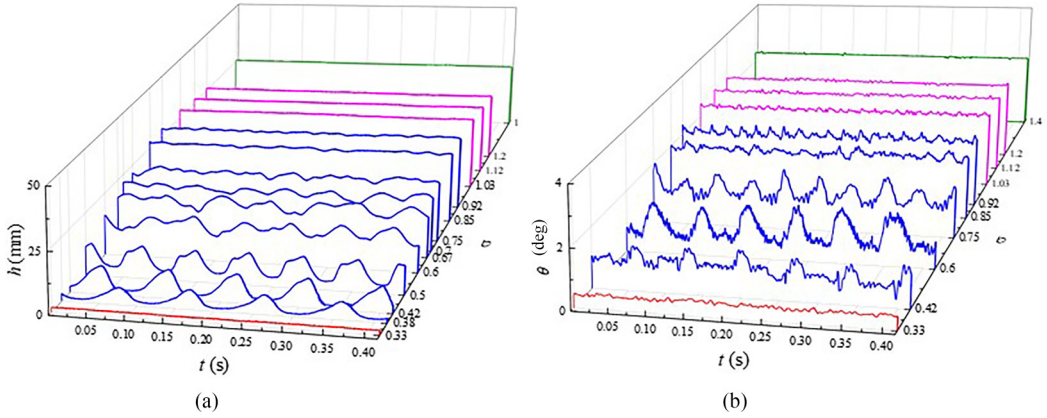


FIG. 4. Evolution of (a) bending deformations and (b) twisting deformations of the flexible hydrofoil at some typical cavitation numbers, where the red, blue, carmine, and green lines represent the supercavitation, cloud cavitation, sheet cavitation, and incipient cavitation regimes, respectively. A relatively small fluctuation of bending and twisting deformations can be observed in the incipient cavitation and sheet cavitation regime due to the steady hydrodynamic load compared with other cavitation stages, and they fluctuate dramatically in the cloud cavitation regime due to the unsteady cloud cavity shedding downstream, causing unsteady hydrodynamic force. The deformation fluctuation decreases obviously when transforming into the supercavitation regime.

The results show a similar trend in the cavity length between rigid and flexible hydrofoils. Both of them increase with the decay of the cavitation number. Moreover, the amplitudes of fluctuations in cavity length of both hydrofoils are small in the incipient cavitation due to the steady cavity and large in-sheet or in-cloud cavitation due to the unsteady periodical shedding and collapse of the cavity. The unsteady cloud cavity loads cause the fluctuation amplitude of bending h and twisting θ deformation to be the largest in the cloud cavitation regime. To provide a further description of the deformations, Fig. 4 shows the evolution of the bending and twisting deformations of the flexible hydrofoil in four typical cavitation regimes. The deformations fluctuate periodically in the cloud cavitation regime due to the periodic shed cloud cavities. However, there are some key differences in the cavity length between the two hydrofoils. The maximum cavity lengths of the flexible hydrofoil over the whole range of cavitation numbers are larger than those of the rigid hydrofoil because the center of pressure shown in Fig. 6 upstream of the hydrofoil elastic axis results in nose-up twist deformation, causing an increase in the effective angle of attack; thus the pressure on the suction side is reduced, and the cavity lengths increase, as shown in Fig. 7. Moreover, the minimum cavity lengths of the flexible hydrofoil over the whole range of cavitation numbers are smaller than that of the rigid hydrofoil. The minimum cavity length occurs when the reentrant jet propagates forward to the farthest distance. This suggests that the intensity of the reentrant jet of the flexible hydrofoil is stronger than that of a rigid hydrofoil.

The side and top views of cavity structures of two hydrofoils in the typical cavitation regimes are shown in Fig. 5. The cavity in the incipient cavitation regime can be observed on the leading edge of the cavity, as shown in Figs. 5(a) and 5(b). Van Rijsbergen [27] suggested that the formation of the incipient cavity was related to five key parameters: free-stream nuclei, roughness elements, surface-bound nuclei, and a laminar separation bubble. It is noted that the incipient cavitation number of the flexible hydrofoil ($\sigma = 1.4$) is larger than that of the rigid hydrofoil ($\sigma = 1.3$), because the nose-up deformation of the flexible hydrofoil results in an increase in the effective angle of attack, as shown in the lower-right region of Fig. 3. The mean value of the twisting deformation θ of the flexible hydrofoil reaches 2.3° at $\sigma = 1.4$. The greater the angle of attack is, the earlier cavitation occurs. Further decreasing the cavitation number, the length of the cavity grows longer, and it is

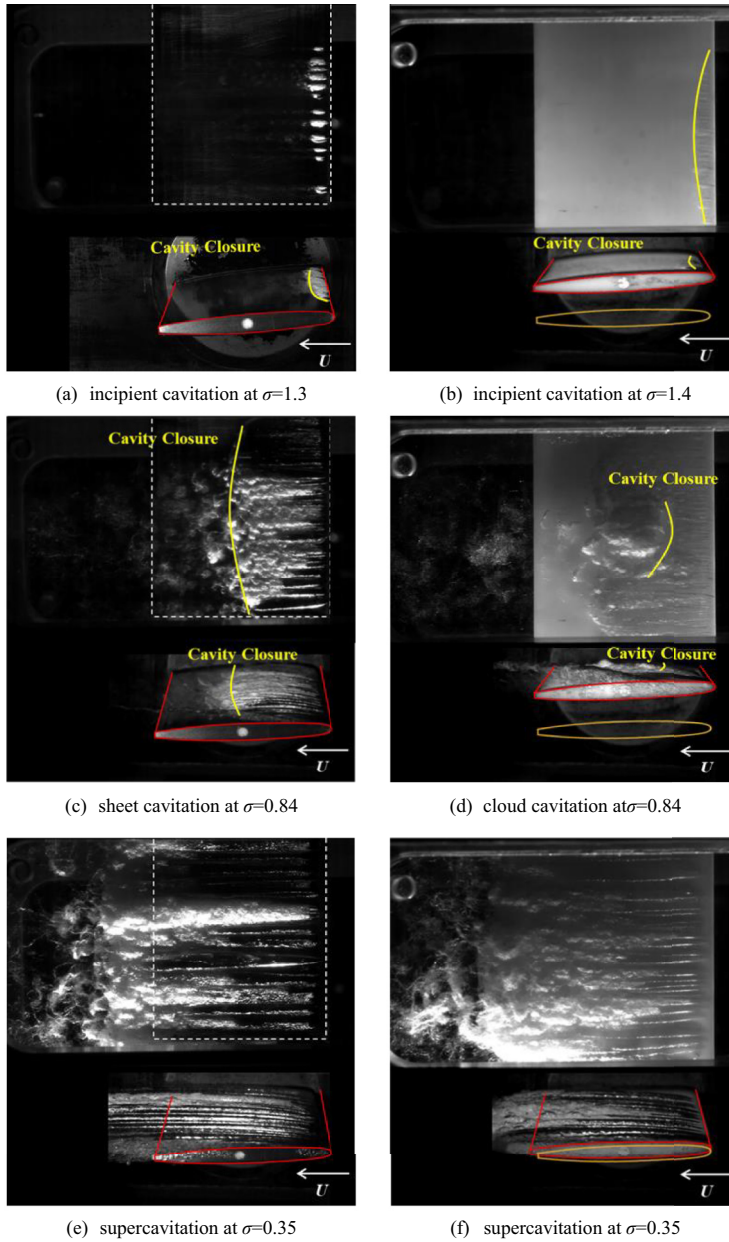


FIG. 5. Cavity structures of the rigid (left column) and flexible hydrofoil (right column) at typical cavitation numbers. The outline of the hydrofoil shown in yellow is the initial position of the flexible hydrofoil, and that shown in red is the position of the hydrofoil at the current time. The yellow lines in the top view of the images represent the cavity closure, and it is concave due to the forward propulsion of the reentrant jet.

often accompanied by a highly unsteady trailing edge, as shown in Fig. 5(c). When the trailing edge becomes increasingly unsteady, cloud cavitation is formed. In cloud cavitation, vortex shedding into the downstream flow field appears at certain frequencies. The sheet or cloud cavitation of the flexible hydrofoil experienced a greater range of cavitation numbers than that of the rigid hydrofoil,

which indicates that the flexible hydrofoil accelerates the transition between cavitation regimes for decreasing σ . Note that the difference in the maximum cavity length between two hydrofoils is the largest at $\sigma = 0.8$. This is because the effective angle of attack of the flexible hydrofoil is larger than that of the rigid hydrofoil, resulting in lower pressure on the suction side. Thus, the flexible hydrofoil turns into the cloud cavitation regime at $\sigma = 0.84$, while the rigid hydrofoil is still in the sheet cavitation regime. The shedding large-scale cloud cavity structures of the flexible hydrofoil can be seen at $\sigma = 0.84$, while stable sheet cavitation accompanied by an unsteady trailing edge can be observed for the rigid hydrofoil at $\sigma = 0.80$. With a further decrease in the cavitation number, the two hydrofoils turn into the supercavitation regime. In this regime, the pressure in the cavitating area is low and a big fixed cavity is formed, which is longer than the chord length of the hydrofoil. Compared with other types of cavitation, the interface of a supercavitation cavity is stable, as shown in Figs. 5(e) and 5(f). The critical cavitation number between the cloud cavitation and supercavitation regimes of the flexible hydrofoil ($\sigma = 0.38$) is slightly smaller than that of the rigid hydrofoil ($\sigma = 0.40$). The cavity length of the rigid hydrofoil remains stable, while the flexible hydrofoil fluctuates violently in the supercavitation regime. It can be seen from the cavity structures of the two hydrofoils at $\sigma = 0.35$ that the cavity of the flexible hydrofoil sheds and collapses downstream. This phenomenon is related to the influence of FSI on the cavitating flow, especially the structural vibration.

Figure 6 shows the mean value of the lift \bar{C}_L , drag \bar{C}_D , and moment \bar{C}_{MZ} coefficients; lift-drag ratio $\bar{K} = \bar{C}_L/\bar{C}_D$; location of the center of pressure $\bar{x}_p/c = 0.5 - \bar{C}_{MZ}/\bar{C}_L$; and standard deviation values of lift C'_L , drag C'_D , and moment coefficients C'_{MZ} of the rigid and flexible hydrofoil at various σ , where \bar{x}_p/c gives the center of action of the forces acting along the hydrofoil from the leading edge. The first layer of Fig. 6 shows that the trends of the lift coefficients of the two hydrofoils are similar, and this trend is in good agreement with other studies [28,29]. The lift coefficients of the two hydrofoils both remain constant in the subcavitation and then increase slightly from incipient cavitation to a typical cavitation number ($\sigma = 0.92$ for the flexible hydrofoil and $\sigma = 0.75$ for the rigid hydrofoil), which is exactly their boundary between sheet cavitation and cloud cavitation. Subsequently, the lift coefficients decrease with the decay of the cavitation number. The reason for this has been explained clearly in our previous investigation [26]. Two main factors influence the trend of the lift coefficient with cavitation numbers: the minimum pressure on the pressure side limited by the cavitation number and the effective camber of the cavitating hydrofoil. The latter is dominant when the cavitation number is larger because the cavity structure changes greatly with decreasing cavitation number. In addition, as the cavitation decreases, the pressure on the suction side decreases. It causes an increase in the pressure difference between the pressure side and the suction side. However, the former is dominant when the cavitation number is smaller because the cavity length nearly exceeds the trailing edge of the hydrofoil, so the influence of the camber decreases. While the pressure side of the hydrofoil decreases with the reduction of cavitation number, so the pressure difference between the pressure side and the suction side decreases.

Note that when the cavitation number is larger, the lift coefficient of the flexible hydrofoil is larger than that of the rigid hydrofoil, because the center of pressure upstream of the hydrofoil elastic axis results in a positive moment, leading to nose-up twist deformation, causing an increase in the effective angle of attack, which causes an increase in the lift, as shown in Fig. 7. The variation of lift with the angle of attack has been studied in our previous work [18]. Then the difference between them almost disappears when the cavitation number is smaller than 0.76 due to the decrease in twisting deformation of the flexible hydrofoil. The second layer of Fig. 6 shows the drag coefficients of the two hydrofoils. In the subcavitation regime, the drag is mainly caused by the frictional resistance between the surface of the foil and the inlet flow. As the cavitation number decreases, it begins to transform into the sheet or cloud cavitation regime, and the trailing edge of the hydrofoil becomes unstable, causing detachment of the cavity and flow, resulting in an increase in shape resistance. The frictional resistance decreases as the cavity area increases because the viscosity coefficient of vapor is much smaller than that of liquid. The shape resistance is dominant in this stage, so the drag coefficients of the two hydrofoils both increase from subcavitation to a typical

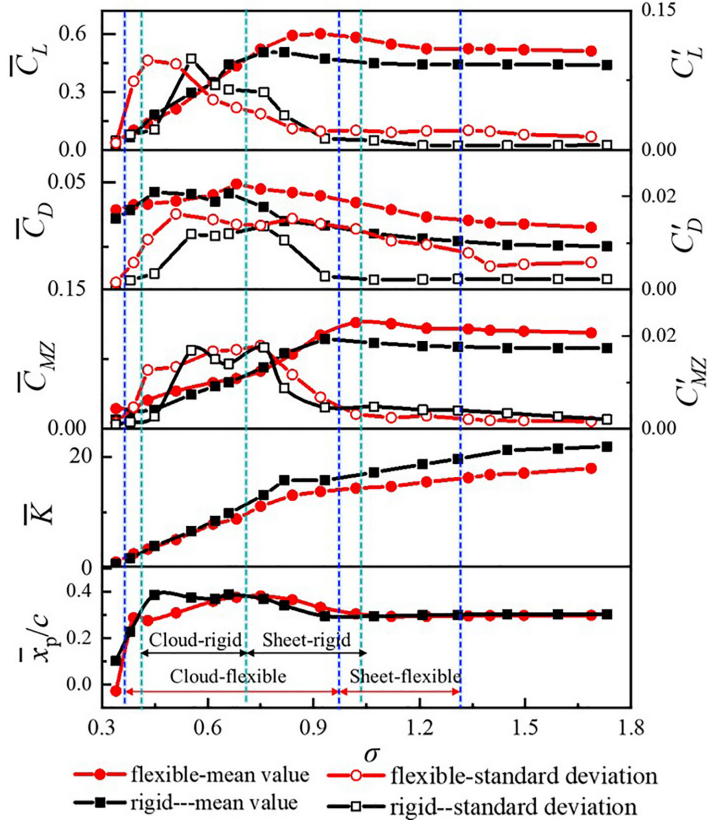


FIG. 6. Measured mean values of the lift \bar{C}_L , drag \bar{C}_D , and moment coefficients \bar{C}_{MZ} ; efficiency \bar{K} ; location of the center of pressure \bar{x}_p/c (solid points); and standard deviation values of lift C'_L , drag C'_D , and moment coefficients C'_{MZ} (circles) at various σ of the rigid and flexible hydrofoil. The results show that the trends of the mean values of \bar{C}_L , \bar{C}_D , and \bar{C}_{MZ} of the two hydrofoils are the same, while those of the flexible hydrofoil are all larger than those of the rigid hydrofoil due to a strong FSI influence.

cavitation number in the cloud cavitation. Note that the drag coefficient of the flexible hydrofoil is larger than that of the rigid hydrofoil in this range of cavitation numbers due to the larger shape resistance. When it transforms into supercavitation, the stable cavity causes a reduction in shape resistance. The moment coefficients first remain constant and then decrease with the reduction in σ because of the decrease in the lift coefficient when the cavitation number is smaller, although the moment arm increases due to the approach of \bar{x}_p/c to the leading edge. The larger lift of the flexible hydrofoil causes the moment coefficients to be larger than that of the rigid hydrofoil at larger cavitation numbers regions, as shown in Fig. 7. In addition, the lift-drag ratio of the flexible hydrofoil is smaller than that of the rigid hydrofoil when σ is larger than 0.62 and nearly the same as that of the rigid hydrofoil when σ is smaller than 0.62. The standard deviations of the lift, drag, and moment coefficients of both rigid and flexible hydrofoils are the largest in the sheet or cloud cavitation regime due to the unsteady cavity. It is interesting to observe that both the drag and moment coefficients reach the maximum standard deviation value at $\sigma = 0.75$, while the lift coefficient reaches the maximum value at $\sigma = 0.55$ for the rigid hydrofoil. For the flexible hydrofoil, the lift, drag, and moment coefficients reach their maximum values at $\sigma = 0.43$, $\sigma = 0.51$, and $\sigma = 0.75$, respectively. The cavitation number is the same when the standard deviations of bending deformation and lift coefficient of the flexible hydrofoil reach the maximum value, suggesting that

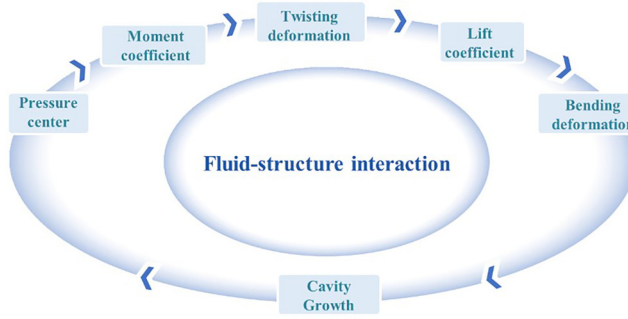


FIG. 7. Schematic of the interaction among the cavity dynamics, hydrodynamic loads, and deformations due to fluid-structure interaction.

the bending deformation is positively correlated with the lift coefficient. The standard deviation of the moment coefficient reaches its maximum earlier than that of the lift coefficient.

The standard deviation of the lift coefficient and bending deformation of the flexible hydrofoil reach the maximum value at the same cavitation number ($\sigma = 0.42$), suggesting a strong relationship between hydrodynamic loads and deformations due to FSI. To investigate the relationship between the load and deformations, Fig. 8 shows the relationship between lift coefficients and bending deformations, together with moment coefficients and twisting deformations of the flexible hydrofoil at different cavitation numbers. The results show that the hydrodynamic loads and deformations reach the maximum value in the sheet or cloud cavitation regime and reach the minimum value in the supercavitation regime. In addition, large fluctuations of the deformation and loads can be observed in the cloud cavitation regime. Figure 8(a) shows that lift is positively correlated with bending deformation. This indicates that bending deformation is mainly determined by the lift. Figure 8(b) shows that the moment is positively correlated with twisting deformation, suggesting that the twisting deformation is mainly dependent on the moment. Thus, the trend of bending deformation with cavitation number is the same as that of the lift coefficient. Both of them reach the largest value at $\sigma = 0.92$. The correlation between lift and bending deformation can be fitted by a linear function $\bar{C}_L = 0.02 \times \bar{h} + 0.03$. The trend of twisting deformation with cavitation

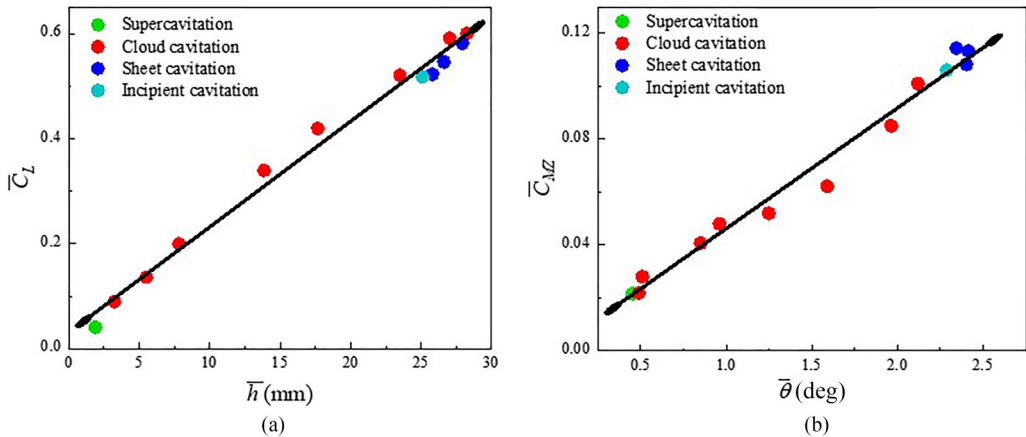


FIG. 8. Relationship between (a) lift coefficient and bending deformation and (b) moment coefficient and twisting deformation of the flexible hydrofoil. The points represent the mean value of load coefficients and deformations at different cavitation numbers, and the lines represent linear functions fitted to these points.

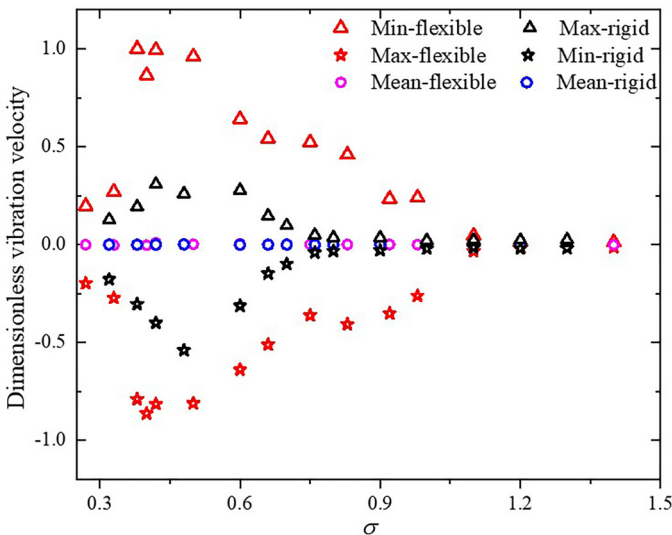


FIG. 9. Measured mean, maximum, and minimum vibration velocities of the rigid and flexible hydrofoil at various cavitation numbers. The blue and green areas represent the cavitation number range of the cloud cavitation regime for the flexible and rigid hydrofoils, respectively. The fluctuation amplitudes of the rigid and flexible hydrofoil reach the largest values at $\sigma = 0.38\text{--}0.50$ and $\sigma = 0.42\text{--}0.60$, respectively. The maximum and minimum values of the vibration velocity of the flexible hydrofoil are much larger than those of the rigid hydrofoil in the cloud cavitation regime.

number is the same as the moment coefficient. Both of them reach the largest value at $\sigma = 1.12$. The relationship between the moment and twisting deformation can be fitted by a linear function $\bar{C}_{MZ} = 0.046 \times \bar{\theta} + 0.00026$.

In addition to deformations, vibration characteristics are another important factor in studying FSI on the structure response. Figure 9 shows the dimensionless structural vibration velocities measured by a portable laser vibrometer in statistical characteristics between two hydrofoils, including mean, maximum, and minimum values. The amplitude of the structural vibration velocity is normalized by the maximum value of the flexible hydrofoil. The results show that the mean values of rigid and flexible hydrofoils are both close to zero, indicating that the vibration velocity is symmetrical at all cavitation regimes. The cavitation number when the fluctuation amplitude of vibration velocity reaches the peak is consistent with that when the standard deviation of the lift coefficient reaches the maximum value for both hydrofoils, suggesting that the vibration velocity mainly depends on the lift. In addition, the fluctuation of the flexible hydrofoil is much larger than that of the rigid hydrofoil in the cloud cavitation stage, indicating the stronger influence of cavitation on a flexible hydrofoil than on a rigid hydrofoil.

To further investigate the difference in vibration features between the two hydrofoils, Fig. 10 shows the evolution of vibration velocity for rigid and flexible hydrofoils at typical cavitation numbers. The results show that the fluctuation is the largest and quasiperiodic in the cloud cavitation stage due to the unsteady shedding cavity, while in the other stages, only a small fluctuation can be seen. In addition, the amplitude of the vibration velocity for the flexible hydrofoil is much larger than that for the rigid hydrofoil at the same cavitation number. It indicates the cavity dynamics of flexible hydrofoils has a stronger effect on the structural response.

Spectrograms of vibration velocity of the rigid and flexible hydrofoil for a range of σ are shown in Figs. 11 and 12. Three main peaks are captured for the rigid hydrofoil, the cavity shedding frequency f_{cav} , the system-related frequency f_{sys} , and the wake vortex shedding frequency f_{vor} . A detailed illustration is given in our previous work [26]. Compared to the rigid hydrofoil, only the

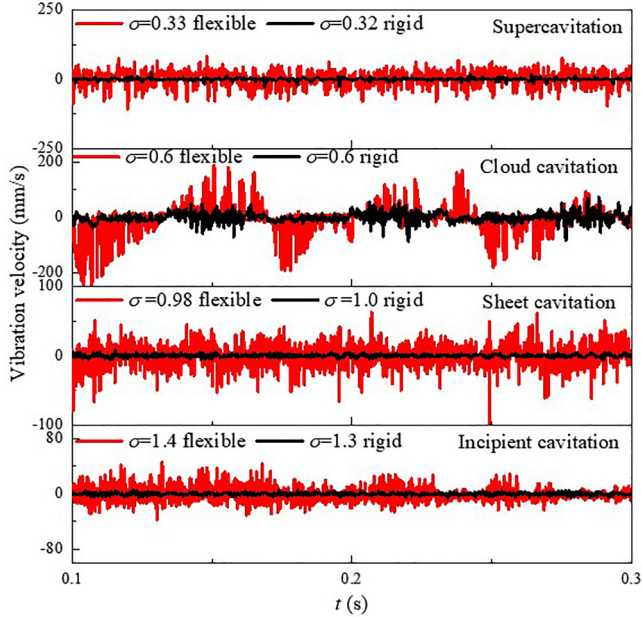


FIG. 10. Comparison of vibration velocity between rigid and flexible hydrofoils at typical cavitation numbers. The four stack diagrams are supercavitation, cloud cavitation, sheet cavitation, and incipient cavitation from top to bottom. The scale of each stack diagram is the same, from -250 to 250 mm/s. $\sigma = 1.40$ and $\sigma = 1.30$ are the incipient cavitation numbers of the flexible and rigid hydrofoils, respectively.

cloud cavity shedding frequency of the flexible hydrofoil can be seen in the frequency spectrogram. It suggests that the flexible hydrofoil appears to dampen higher-frequency oscillations due to its lower natural frequency. The vibration and deformation lead to the cavitation being more intense,

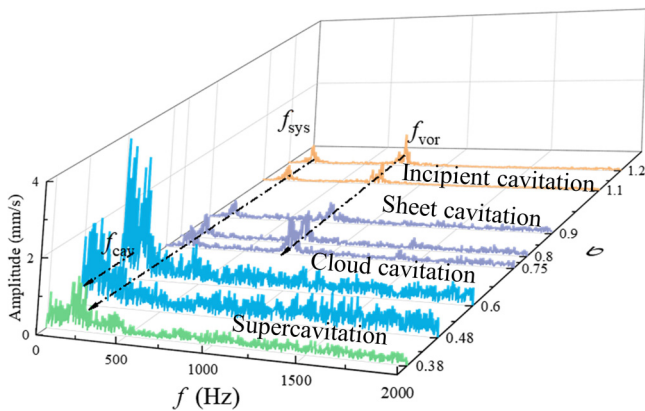


FIG. 11. Spectrogram of vibration velocity for a range of σ for the rigid hydrofoil [26]. The dominant frequency peak f_{cav} is evident in the cloud cavitation regime, which corresponds to the cloud cavity shedding frequency. Another main peak in the spectrogram f_{sys} appears in the whole range of cavitation numbers and is independent of σ being equal to 160 Hz, which is supposed to be the system-related frequency. Another peak f_{vor} is related to the wake vortex shedding frequency with a Strouhal number of 0.23 , which is in good agreement with that of the Kármán vortex by Aousni [7].

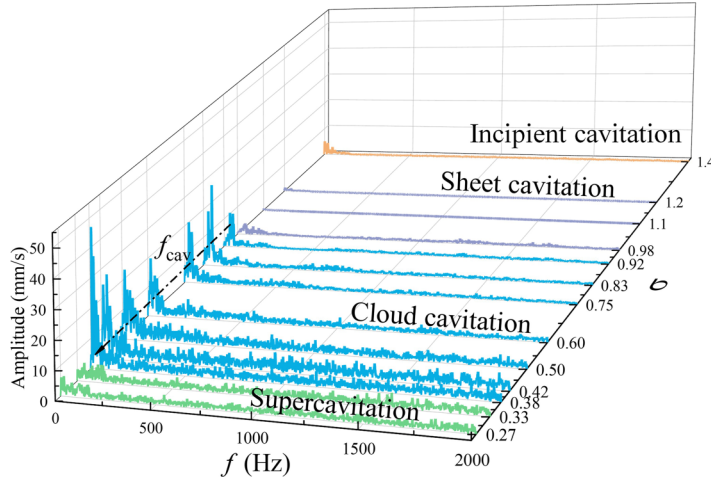


FIG. 12. Spectrogram of vibration velocity for a range of σ for the flexible hydrofoil. The green, blue, purple, and orange lines represent supercavitation, cloud cavitation, sheet cavitation, and incipient cavitation, respectively. The amplitude of the dominant frequency of the flexible device is much larger than that of the rigid device.

which hinders the periodic formation and shedding of the wake vortex. This shows the significant effect of FSI on structural vibration. The relatively large vibration velocity appears to interfere with the manifestation of induced hydrofoil loading from shedding cloud cavitation, where the flexible hydrofoil appears to dampen higher-frequency oscillations.

It can be seen from spectral analysis that the vibration frequency in the cloud cavitation regime is the most complex and mainly concentrated in low frequencies. Figures 13 and 14 give the vibration

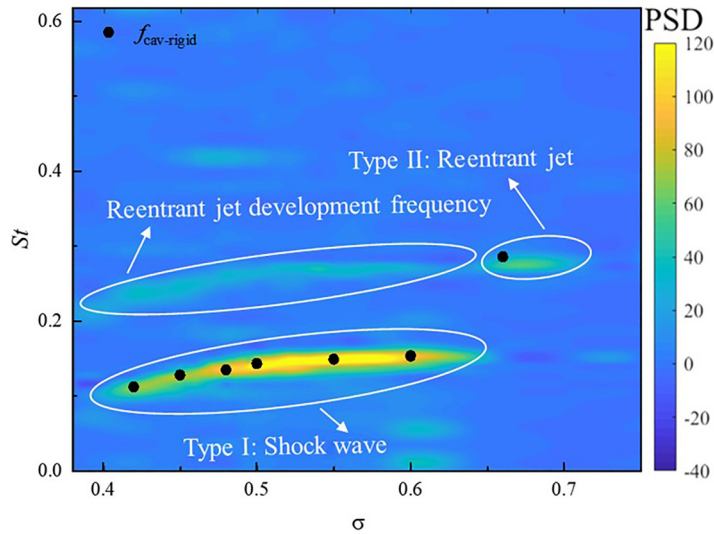


FIG. 13. Spectrum of vibration velocities of the rigid hydrofoil in the cloud cavitation regime. The dark regions of the contour represent some main vibration frequencies. The transition cavitation number from the reentrant jet shedding mechanism (type II) to the shock-wave shedding mechanism (type I) for the rigid hydrofoil is between 0.60 and 0.70.

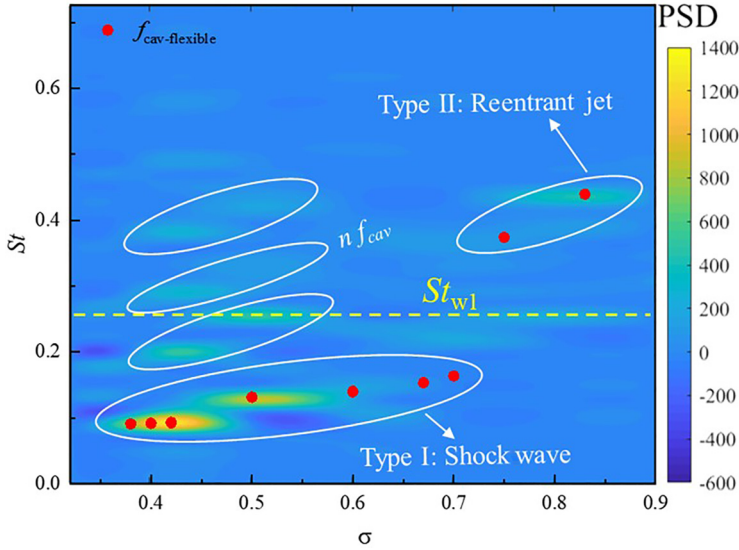


FIG. 14. Spectrum of vibration velocities of the flexible hydrofoil in the cloud cavitation regime. The transition cavitation number from the reentrant jet shedding mechanism (type II) to the shock-wave shedding mechanism (type I) is between 0.70 and 0.75. The natural frequency in fully wetted water is shown as a yellow dotted line.

velocity spectra showing low-frequency information in the cloud cavitation regime from $\sigma = 0.38$ to 0.75 for the rigid hydrofoil and from $\sigma = 0.32$ to 0.90 for the flexible hydrofoil. The spectra of the vibration velocity of both hydrofoils are constructed from spectra at 0.05 increments of σ . The spectra are obtained by the Fourier transform of the envelope smoothed with five points. Frequency is nondimensionalized as a chord-based Strouhal number, $St = fc/U_\infty$. The red and black points represent the large-scale cloud cavity shedding frequencies of the flexible and rigid hydrofoil, respectively. They are obtained by the fast Fourier transform of the cavity area pixels of the gray images with further details that can be found in Liu *et al.* [18]. The Strouhal numbers of the flexible and rigid hydrofoils both decrease as the cavitation number decreases. The most obvious tonal peaks agree well with the cloud cavity shedding frequencies, suggesting that the cloud cavity shedding frequency dominates the structural response due to the fluid-structure interaction. Another distinct frequency band can be observed in the contour of the rigid hydrofoil at smaller cavitation numbers, which are related to the reentrant jet development frequency, because this band is connected to the band of cloud cavity shedding frequency induced by the reentrant jet mechanism at larger cavitation numbers.

Moreover, at a certain cavitation number, the St of rigid and flexible hydrofoils shows a sharp drop. This sharp drop in St may be attributed to the transition of the cloud cavity shedding mechanism from the reentrant jet mechanism (type II) to the shock-wave mechanism (type I). More details about these two shedding mechanisms will be explained later in Sec. III B. A sudden and dramatic change in frequency of the rigid hydrofoil can be seen from $\sigma = 0.60$ to $\sigma = 0.70$ from Fig. 13. Note that this sharp drop of the flexible hydrofoil appears earlier than that of the rigid hydrofoil, as shown in Fig. 14. It indicates that the flexible hydrofoil accelerates the transition from the reentrant jet shedding mechanism to the shock-wave mechanism with a decrease in cavitation number. In addition, the cavity shedding frequency of the flexible hydrofoil is lower than that of the rigid hydrofoil, because the transient cavity loads induce nose-up twist deformation of the flexible hydrofoil due to the fluid-structure interaction, which increases the effective angle of attack, leading to longer cavity length. Hence it requires more time to evolve between the subsequent cycles, as

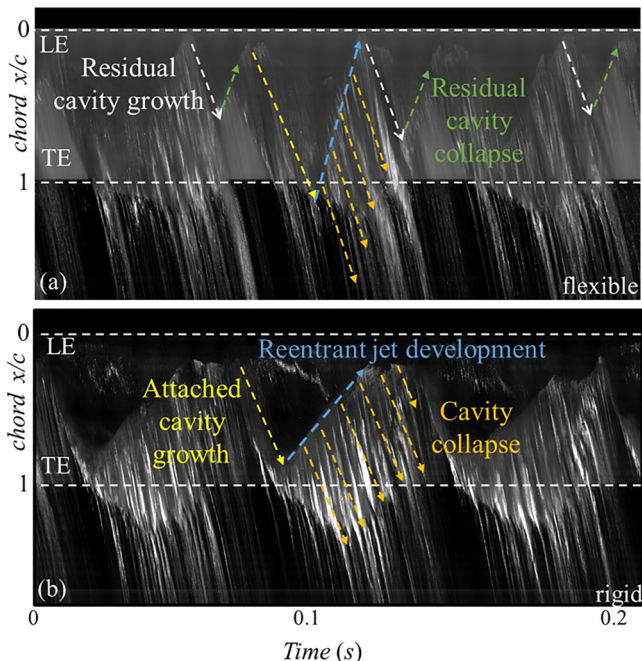


FIG. 15. Chordwise space-time diagram characteristic of the time dependence of the cavity for (a) flexible and (b) rigid hydrofoil at $\sigma = 0.50$. The process of cloud cavity shedding of the rigid hydrofoil induced by the shock-wave mechanism is composed of attached cavity growth, reentrant jet development (blue lines), cavity shedding, and collapse (orange lines). Compared with the rigid hydrofoil, the shedding process of the flexible hydrofoil has one more residual cavity development (white lines) and collapse process (green lines) due to the stronger shock wave.

shown in Fig. 7. In addition to the cavity shedding frequency $f_{\text{cav-POM}}$ being captured by the vibration frequency analysis, double cavity shedding frequency $n f_{\text{cav-POM}}$ can also be seen. Furthermore, the first-order modal natural frequency in fully wetted water [30] ($f_{w1-\text{POM}} = 32$ Hz) of the flexible hydrofoil is excited in cavitating flow.

B. Cavity dynamics in the cloud cavitation regime

To provide a detailed explanation of why the cavity shedding frequency of the flexible hydrofoil is less than that of the rigid hydrofoil, Fig. 15 shows the chordwise space-time diagram characteristic of the time dependence for two hydrofoils at $\sigma = 0.50$. The chordwise space-time diagrams for both hydrofoils illustrate how the cloud cavitation varies along the chord over time. It is composed of several shedding cycle pixels extracted from the midspan of the gray profile of the top view. More details about the chordwise space-time diagram are shown in our previous work [18]. The results show that the flexible hydrofoil has one more secondary growth (white dotted line) and shedding (green dotted line) process of the attached cavity than the rigid hydrofoil during one shedding cycle, which proves the existence of the shock wave [14,19,23,26,31]. The increase in twisting deformation leads to an increase in the angle of attack, leading to a more intense shock wave of the flexible hydrofoil. It is well known that the sound speed of high-void-fraction cavitation bubbly mixtures is greatly reduced compared to that of the constituent water, air, and vapor [32]. This makes such mixtures compressible and susceptible to shock under certain flow conditions. When the average Mach number of the cavity flow exceeds that required for the generation of strong shocks, the front shock propagates upstream with high pressure, causing the residual sheet cavity to turn into

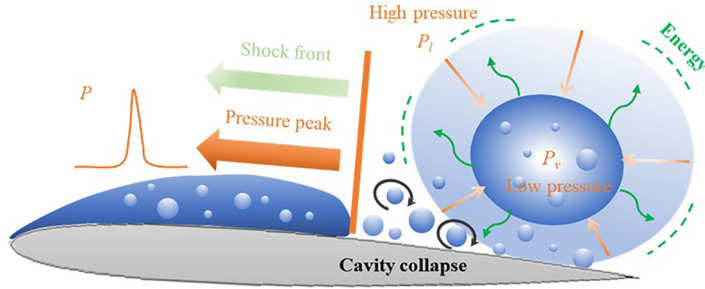


FIG. 16. Schematic of shock-wave formation and propagation. The increase in the pressure difference between the inside and the outside causes the cavity to collapse and release large amounts of energy. The pressure spike propagates forward, resulting in the collapse of the attached cavity.

the bubbly region and then collapse immediately [33,34]. The Mach number is defined as $M_{FL} = U_{FL}/C_{1s}$ [32], where C_{1s} represents the sound speed of the cavitating flow upstream of the observed shocks. The speed of sound in air-water mixture according to the volume fraction of the air. U_{FL} is the front speed of the shocks in the laboratory frame. The shock-wave propagation is related to the collapse of the shed cloud cavity [35], as shown in Fig. 16. When the cavity moves to the high-pressure region, the vapor volume fraction of the cavity decreases rapidly, and the pressure difference between the inside and outside of the cavity increases gradually, so the cavity collapses quickly.

Thus, we surmise that the shed cloud cavity void fraction of the flexible hydrofoil is larger than that of the rigid hydrofoil, generating a stronger shock wave and releasing more energy to cause the residual attached cavity to collapse. This is the reason why the minimum cavity length of the flexible hydrofoil is smaller than that of the rigid hydrofoil, as shown in Fig. 3. More details about the comparison of the shedding process for the two hydrofoils are shown in Fig. 17.

Figure 17 shows the evolution of the cloud cavity shedding process induced by the shock-wave mechanism for rigid and flexible hydrofoils during one typical cavitation cycle at $\sigma = 0.50$. At $t_1 = t_0$, it is the beginning of the attached cavity growth, and the attached cavity reaches the minimum length l_1 and l'_1 for the rigid and flexible hydrofoil, respectively. From t_1 to t_2 , the development of the attached cavity can be observed for the two hydrofoils. At $t_2 = t_0 + 32\%T_1$, the attached cavity develops at the trailing edge of the hydrofoil, and the reentrant jet forms in the cavity closure. From t_2 to t_4 , the reentrant jet develops from the cavity closure toward the leading edge. At $t_3 = t_0 + 50\%T_1$, frothy bubbles can be seen in the area through which the reentrant jet flows, which is due to the collision between the reentrant jet and the cavity surface. At $t_4 = t_0 + 71\%T_1$, the reentrant jet develops the forefront, and the adverse pressure gradient is too large to pinch off the sheet cavity from the cloud cavity. The large-scale cloud cavity can be seen near the trailing edge of the hydrofoil. The length of the sheet cavity for the flexible hydrofoil l_2 is shorter than that of the rigid hydrofoil l'_2 , which indicates that the speed of the reentrant jet for the flexible hydrofoil is faster than that for the rigid hydrofoil. From t_4 to t_5 , the sheet cavity of the rigid hydrofoil is reduced from l'_2 to l'_3 by the shock wave. The sheet cavity of the flexible hydrofoil grows from l_2 to l_3 because the shedding of the cloud cavity downstream provides space for the development of the residual sheet cavity. At $t_5 = t_0 + 87\%T_1$, the residual sheet cavity develops to its maximum length l_3 . From t_5 to t_6 , the residual sheet cavity continues to decrease due to the effect of the shock wave. At $t_6 = t_0 + T_1$, the residual cavity is reduced to the minimum length l'_4 and l_4 for the rigid and flexible hydrofoil, respectively, which indicates the shock wave of the flexible hydrofoil is more intense than that of the rigid hydrofoil.

It is well known that cloud cavitating flows are quasiperiodic [36–38]. To provide further information on the difference between the two hydrofoils from a global perspective, the mean flow field and the first two Proper Orthogonal Decomposition (POD) modes of rigid and flexible

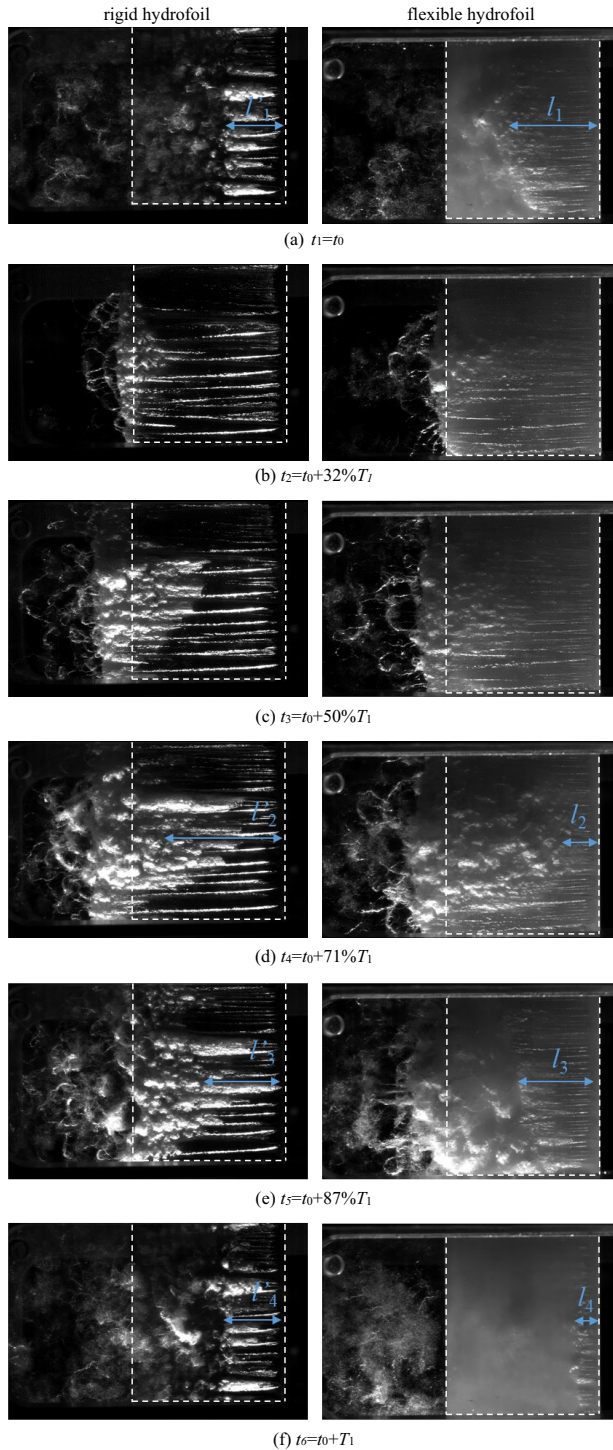


FIG. 17. Time evolution of cloud cavitation patterns induced by the shock-wave mechanism at $\sigma = 0.50$ for rigid (left) and flexible (right) hydrofoils. The blue lines represent the attached cavity length. T_1 represents the shock-wave -induced cloud cavity shedding periods of two hydrofoils.

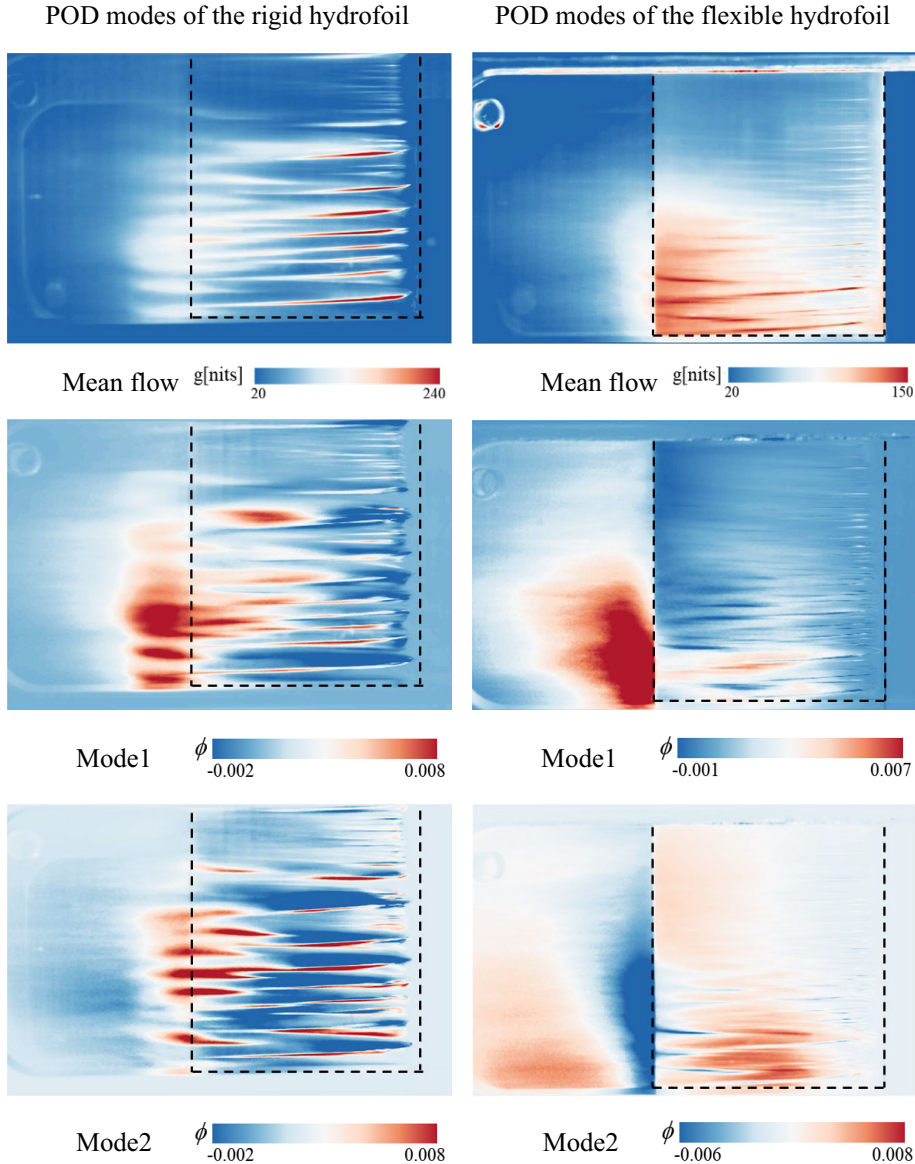


FIG. 18. Mean flow and the first two energetic POD modes of the rigid (left) and flexible (right) hydrofoil at $\sigma = 0.50$. The figures in the first line represent the mean flow. g represents the gray value and ϕ is the POD mode, which represents the dominant structure of the flow field. The first two POD modes represent the large-scale structure of the cavitating flow.

hydrofoils are shown in Fig. 18. In this work, the gray values of the unsteady cloud cavitating field constitute a $K \times N$ matrix P , where K (number of mesh elements) = 172032 and N (snapshots counts) = 800. Each value in the column corresponds to the gray value of the experimental images.

The first row of Fig. 18 shows the mean flow field of the rigid and flexible hydrofoils. The leading edge of the attached cavity of the rigid hydrofoil exhibits a fingerlike structure. Compared with the rigid hydrofoil, the root of the attached cavity of the flexible hydrofoil seems more even, while the tip of the attached cavity exhibits some fingerlike structures. The first two POD modes of the two

hydrofoils at $\sigma = 0.50$ are shown to provide spatial information on the main concentration of cavity shedding. The activity of the first modes of the two hydrofoils is confined to the trailing edge of the hydrofoil, suggesting that the first mode is related to the large-scale cloud cavity, and it occupies the most energy in the whole unsteady cavitating flow. It is obvious that the positive region of the flexible hydrofoil is larger than that of the rigid hydrofoil, which indicates that the flexible hydrofoil forms a larger-scale cloud cavity. This is evidence that the strength of the shock wave of the flexible hydrofoil is larger than that of the rigid hydrofoil. In addition, the first mode energies of the rigid and flexible hydrofoils account for 40.92% and 32.95%, respectively. In conjunction with contour, the results show that the greater the unsteadiness is, the larger the percentage of energy. Mode 2's activity of the flexible hydrofoil is mainly concentrated on the trailing edge of the hydrofoil, while its structure is smaller than mode 1. There are some positive structures downstream, which are related to the shed cavity. The structure of mode 2 of the rigid hydrofoil resembles that of mode 1, except that it is smaller in scale. It is clearer downstream than the flexible hydrofoil. Because the cloud cavity of the rigid hydrofoil collapses in the trailing edge, it disappears downstream. In addition, the second mode energies of the rigid and flexible hydrofoils account for 15.02% and 16.71%, respectively, indicating that the unsteadiness of the flexible hydrofoil is greater than that of the rigid hydrofoil.

IV. CONCLUSIONS

The influence of FSI on the cavity dynamics and structural response is investigated through a comparison of simultaneous high-speed camera visualization, vibration, and lift measurements on rigid and flexible hydrofoils. The dynamic structural behavior plays a significant role in cavity dynamics. The increase in the effective angle of attack of the flexible hydrofoil has the added effect of increasing the cavity length, leading to a reduced cloud cavity shedding frequency, accelerating the formation of incipient cavitation, and causing an early transition from the incipient cavitation regime to the sheet or cloud cavitation regime and from the reentrant jet mechanism to the shock-wave mechanism with the reduction in σ .

Cavitation has a significant effect on structural vibration. The dominant vibration frequency is related to the cloud cavity shedding frequency for both hydrofoils due to the effect of FSI. Compared with the rigid hydrofoil, the vibration of the flexible hydrofoil dampens higher-frequency oscillations. The cloud cavity shedding process of the flexible hydrofoil driven by the shock-wave mechanism has one more secondary growth and shedding process of the attached cavity compared with the rigid hydrofoil. It indicates that the shock wave of the flexible hydrofoil is stronger than that of the rigid hydrofoil.

In this context, the experimental results presented in this paper can be useful in the understanding of complex flow features and structure response, and they can also be useful for the validation of these methods. Much work is still to be done for a good understanding of FSI in cavitating flow. Specific numerical coupled procedures need to be developed and can be useful in the understanding of this interaction. In particular we can use the numerical method to calculate the Mach numbers within the cavity to show more quantitative proofs for the shock wave.

ACKNOWLEDGMENTS

The authors gratefully acknowledge the great help of Prof. Mohamed Farhat (EPFL-LMH) and the strong support provided by the Natural Science Foundation of Beijing Municipality (No. 3232033), the Fundamental Research Funds for the Central Universities (No. 2023CX01004), and the National Natural Science Foundation of China (No. 52279081, No. U22B6010).

- [1] G. Y. Wang, I. Senocak, and W. Shyy, Dynamics of attached turbulent cavitating flows, *Prog. Aerosp. Sci.* **37**, 551 (2001).
- [2] B. Huang, Y. L. Young, and G. Y. Wang, Combined experimental and computational investigation of unsteady structure of sheet/cloud cavitation, *J. Fluids Eng.* **135**, 1 (2013).
- [3] Z. Huang, Y. Xiong, and Y. Xu, The simulation of deformation and vibration characteristics of a flexible hydrofoil based on static and transient FSI, *Ocean Eng.* **182**, 61 (2019).
- [4] A. Peters, U. Lantermann, and O. Moctar, Numerical prediction of cavitation erosion on a ship propeller in model and full scale, *Wear* **408**, 1 (2018).
- [5] A. H. Lee, R. L. Campbell, B. A. Craven, and S. A. Hambric, Fluid-structure interaction simulation of vortex-induced vibration of a flexible hydrofoil, *J. Vib. Acoust.* **139**, 041001 (2017).
- [6] S. Zhang, R. Tian, K. Ding, H. Chen, and Z. Ma, Numerical and experimental study in pressure pulsation and vibration of a two-stage centrifugal pump under cavitating condition, *Mod. Phys. Lett. B* **36**, 2150501 (2022).
- [7] P. Ausoni, M. Farhat, X. Escaler, E. Egusquiza, and F. Avellan, Cavitation influence on von Kármán vortex shedding and induced hydrofoil vibrations, *J. Fluids Eng.* **129**, 966 (2007).
- [8] Z. Wang, H. Cheng, and B. Ji, Numerical prediction of cavitation erosion risk in an axisymmetric nozzle using a multi-scale approach, *Phys. Fluids* **34**, 062112 (2022).
- [9] B. Ji, X. W. Luo, R. E. A. Arndt, X. X. Peng, and Y. L. Wu, Large eddy simulation and theoretical investigations of the transient cavitating vortical flow structure around a NACA66 hydrofoil, *Int. J. Multiphase Flow* **68**, 121 (2015).
- [10] A. Ducoin, J. A. Astolfi, and J. F. Sigrist, An experimental analysis of fluid structure interaction on a flexible hydrofoil in various flow regimes including cavitating flow, *Eur. J. Mech., B: Fluids* **36**, 63 (2012).
- [11] Q. Wu, G. Wang, and B. Huang, Physical and numerical investigation of cavitating flow-induced vibration of a flexible hydrofoil, *Int. J. Fluid Mach. Syst.* **10**, 188 (2017).
- [12] D. T. Akcabay and Y. L. Young, Influence of cavitation on the hydroelastic stability of hydrofoils, *J. Fluids Struct.* **49**, 170 (2014).
- [13] D. T. Akcabay, E. J. Chae, and Y. L. Young, Cavity induced vibration of flexible hydrofoils, *J. Fluids Struct.* **49**, 463 (2014).
- [14] Q. Wu, B. Huang, and G. Y. Wang, Experimental and numerical investigation of hydroelastic response of a flexible hydrofoil in cavitating flow, *Int. J. Multiphase Flow* **74**, 19 (2015).
- [15] A. Lelong, P. Guiffant, and J. A. Astolfi, An experimental analysis of the structural response of flexible lightweight hydrofoils in cavitating flow, *J. Fluids Eng.* **140**, 021116 (2018).
- [16] S. Hu, C. Lu, and Y. He, Fluid-structure interaction simulation of three-dimensional flexible hydrofoil in water tunnel, *Appl. Math. Mech.* **37**, 15 (2016).
- [17] Y. Q. Liao, Viscous fluid–structure interaction response of composite hydrofoils, *Compos. Struct.* **212**, 571 (2019).
- [18] Y. Liu, Q. Wu, and B. Huang, Decomposition of unsteady sheet/cloud cavitation dynamics in fluid-structure interaction via POD and DMD methods, *Int. J. Multiphase Flow* **142**, 103690 (2021).
- [19] S. M. Smith, J. A. Venning, and B. W. Pearce, The influence of fluid–structure interaction on cloud cavitation about a flexible hydrofoil. Part 2, *J. Fluid Mech.* **897**, A28 (2020).
- [20] Y. Q. Liao, J. Martins, and Y. L. Young, Sweep and anisotropy effects on the viscous hydroelastic response of composite hydrofoils, *Compos. Struct.* **230**, 111471 (2019).
- [21] Y. L. Young, Load-dependent bend-twist coupling effects on the steady-state hydroelastic response of composite hydrofoils, *Compos. Struct.* **189**, 398 (2018).
- [22] A. Ducoin and Y. L. Young, Hydroelastic response and stability of a hydrofoil in viscous flow, *J. Fluids Struct.* **38**, 40 (2013).
- [23] Q. Wu, B. Huang, and G. Y. Wang, The transient characteristics of cloud cavitating flow over a flexible hydrofoil, *Int. J. Multiphase Flow* **99**, 162 (2018).
- [24] S. M. Smith, J. A. Venning, and D. R. Giosio, Cloud cavitation behavior on a hydrofoil due to fluid-structure interaction, *J. Fluids Eng.* **141**, 041105 (2018).
- [25] M. Dreyer, Mind the gap: Tip leakage vortex dynamics and cavitation in axial turbines, Ph.D. thesis, École Polytechnique Fédérale de Lausanne, 2015.

- [26] Y. Liu, B. Huang, and H. Zhang, Experimental investigation into fluid–structure interaction of cavitating flow, *Phys. Fluids* **33**, 093307 (2021).
- [27] M. van Rijsbergen, A review of sheet cavitation inception mechanisms, in *16th International Symposium on Transport Phenomena and Dynamics of Rotating Machinery* (ISROMAC, Honolulu, USA, 2016).
- [28] M. M. Karim and M. S. Ahmmed, Numerical study of periodic cavitating flow around NACA0012 hydrofoil, *Ocean Eng.* **55**, 81 (2012).
- [29] H. Ghasemi, Boundary element method applied to the cavitating hydrofoil and marine propeller, *Sci. Iran* **10**, 142 (2003).
- [30] M. Dreyer and M. Farhat, Vortex shedding from a flexible hydrofoil, [arXiv:1110.3355](https://arxiv.org/abs/1110.3355).
- [31] S. M. Smith, J. A. Venning, B. W. Pearce, Y. L. Young, and P. A. Brandner, The influence of fluid–structure interaction on cloud cavitation about a stiff hydrofoil. Part 1, *J. Fluid Mech.* **896**, A1 (2020).
- [32] H. Ganesh, S. A. MäKiharju, and S. L. Ceccio, Bubbly shock propagation as a mechanism for sheet-to-cloud transition of partial cavities, *J. Fluid Mech.* **802**, 37 (2016).
- [33] H. Shamsborhan, O. Coutier-Delgosha, G. Caignaert, and F. Abdel Nour, Experimental determination of the speed of sound in cavitating flows, *Exp. Fluids* **49**, 1359 (2010).
- [34] J. Wu, H. Ganesh, and S. Ceccio, Multimodal partial cavity shedding on a two-dimensional hydrofoil and its relation to the presence of bubbly shocks, *Exp. Fluids* **60**, 66 (2019).
- [35] G. E. Reisman, Y. C. Wang, and C. E. Brennen, Observations of shock waves in cloud cavitation, *J. Fluid Mech.* **355**, 255 (1998).
- [36] G. Chen, G. Wang, and C. Hu, Combined experimental and computational investigation of cavitation evolution and excited pressure fluctuation in a convergent-divergent channel, *Int. J. Multiphase Flow* **72**, 133 (2015).
- [37] W. Liang, T. Chen, and G. Wang, Investigation of unsteady liquid nitrogen cavitating flows with special emphasis on the vortex structures using mode decomposition methods, *Int. J. Heat Mass Transfer* **157**, 119880 (2020).
- [38] C. Xu, R. Field, and S. D. Heister, Modeling cavitating Venturi flows, *J. Propul. Power* **18**, 1227 (2015).